Chapter 4:

Synthesis & Characterization of Rare Earth Doped La_2O_2S: Investigation of It's Optical, Down conversion and Upconversion Properties

Abstract:

The Chapter covers two studies. One is a comparative study of structural data from the XRD spectrum of samples synthesized by three different techniques namely, Solid State Technique, Hydrothermal Technique & Furnace Combustion technique for making Lanthanum Oxysulfide Crystal. The comparative study of reveals that the furnace combustion technique without flux is the best technique as the product has perfect hexagonal lattice with space group 164: $p\bar{3}m1$ and a crystallite size of 31.9 nm. The optical energy band gap of lanthanum oxysulfide synthesized by the furnace combustion technique, calculated from the UV – Visible spectrum is around 4.5 eV. The furnace combustion technique has several advantages that makes it an industrial-friendly approach. It acquired less time for preparation, uses less amount of precursors and doesn't need any pre or post processing. The yield is also high. In the second study, four down conversion samples of 1% Ln^{3+} (Ln = Pr, Eu, Tb, Dy) doped La_2O_2S and six upconversion samples 4% Yb^{3+} - 1% Er^{3+}: La_2O_2S, 12% Yb^{3+} - 2% Er^{3+}: La_2O_2S, 4% Yb^{3+} - 1% Ho^{3+}: La_2O_2S, 12% Yb^{3+} - 2% Ho^{3+}: La_2O_2S, 4% Yb^{3+} - 1% Tm^{3+}: La_2O_2S, 12% Yb^{3+} - 2% Tm^{3+}: La_2O_2S were synthesized by furnace combustion technique. Their structural characteristics as well as optical & photoluminescence properties were investigated. The XRD and EDAX technique was used for structural & elemental analysis. The UV – Visible spectroscopy was used for study of optical properties and the PL spectroscopy was used for photoluminescence studies. The XRD shows that all samples have similar peaks. The peaks match with JCPDS files of hexagonal lattice. EDAX spectra confirmed the incorporation of Ln^{3+} ions in host La_2O_2S. Crystallite size was found to be in nano meter. UV – Visible studies were used to calculate optical band gap, refractive index, absorption wavelength and molar extinction coefficient. The PL excitation

spectra suggest three types of absorption: 4f -5d type absorption in 1% Pr^{3+}: La_2O_2S and 1% Tb^{3+}: La_2O_2S; CTS in 1% Eu^{3+}: La_2O_2S and host absorption in 1% Dy^{3+}: La_2O_2S. Only three samples, 12%Yb^{3+}-2%Er^{3+}: La_2O_2S, 12%Yb^{3+}-2%Ho^{3+}: La_2O_2S, 12%Yb^{3+}-2%Tm^{3+}: La_2O_2S, among the six gave the upconversion photoluminescence.

Keyword: Comparative Study, Furnace combustion technique, XRD, UV – VIS, PL, EDAX

Graphical abstract:

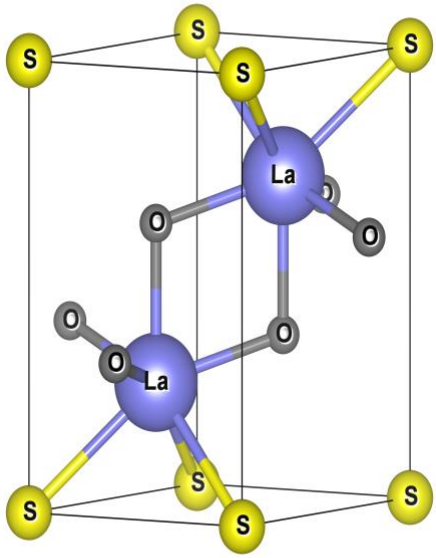

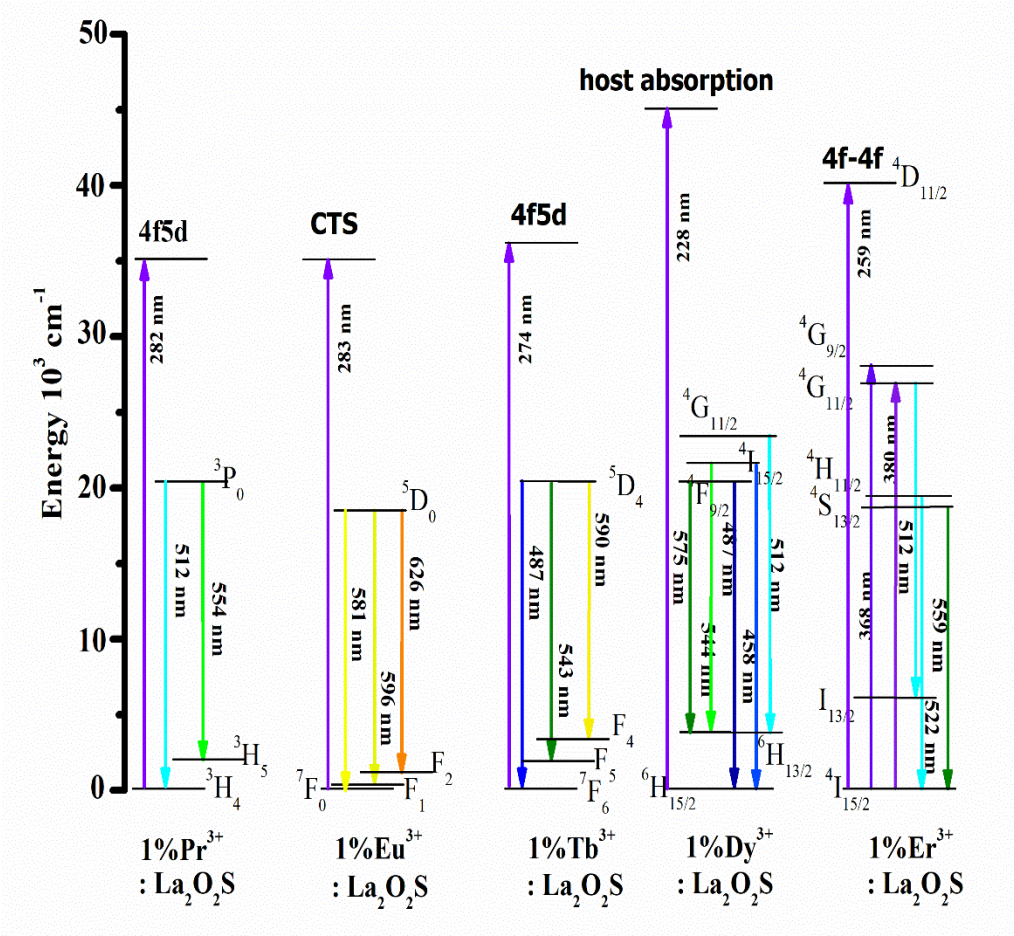
Energy 10^3 cm^{-1}
host absorption
4f5d
CTS
4f5d
4f-4f
282 nm
512 nm
554 nm
283 nm
581 nm
596 nm
626 nm
274 nm
487 nm
543 nm
590 nm
228 nm
575 nm
544 nm
487 nm
458 nm
512 nm
259 nm
368 nm
380 nm
512 nm
559 nm
522 nm
1%Pr^{3+} : La_2O_2S
1%Eu^{3+} : La_2O_2S
1%Tb^{3+} : La_2O_2S
1%Dy^{3+} : La_2O_2S
1%Er^{3+} : La_2O_2S

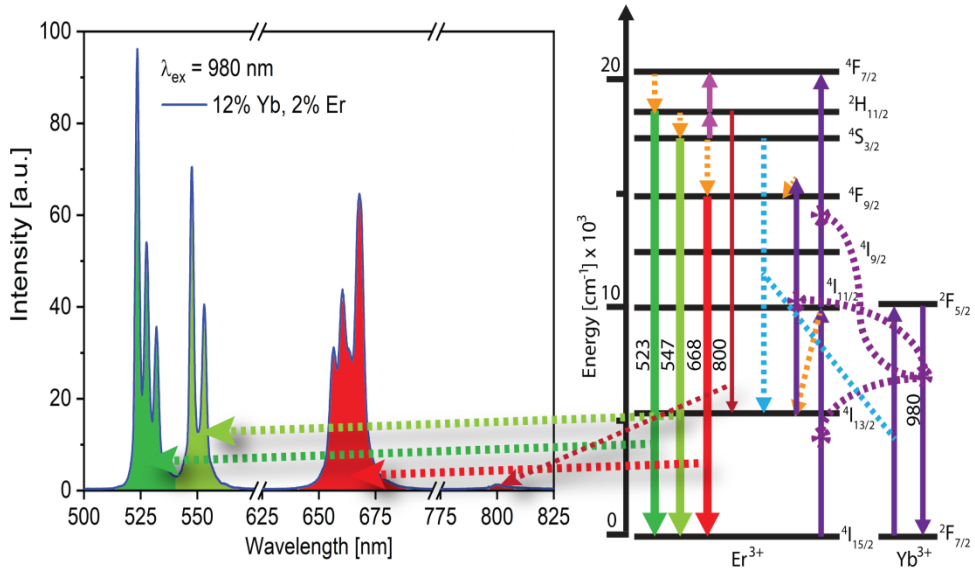
λ_{ex} = 980 nm
12% Yb, 2% Er
Intensity [a.u.]
Wavelength [nm]
Energy [cm^{-1}] x 10^3
523
547
668
800
980
Er^{3+}
Yb^{3+}

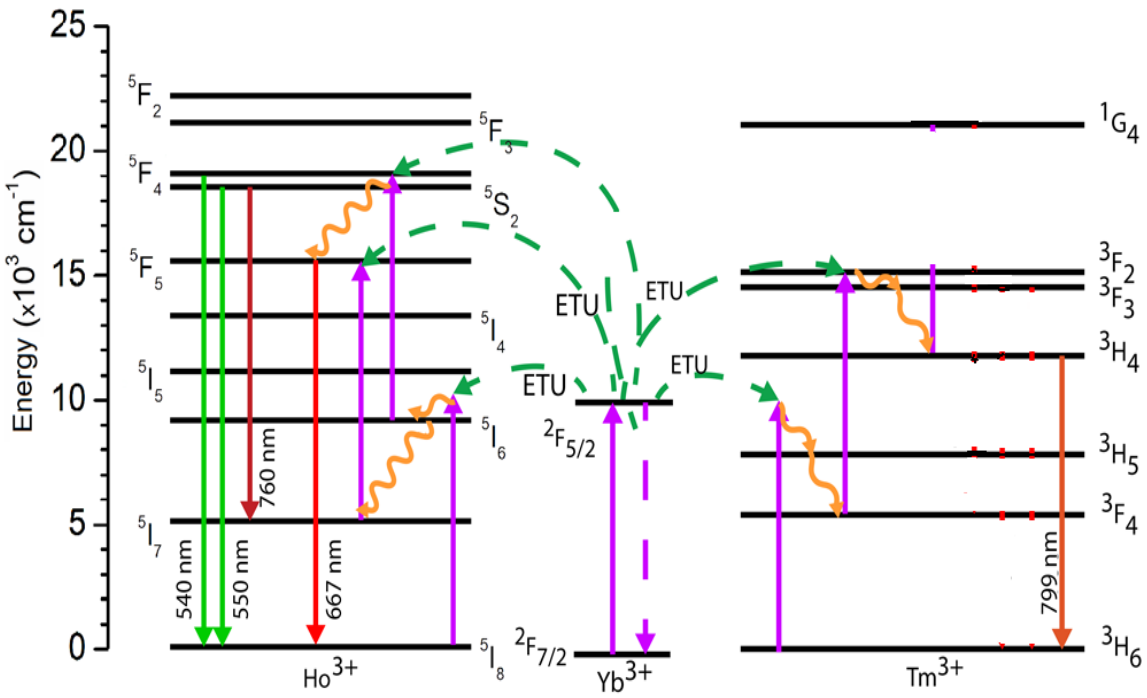

4.1 Introduction:

The dependence of the phenomena of luminescence on material parameters, their co-relation with the spectroscopic transitions, their consequences and their applications have been amply studied[1][2][3][4][5][6] [7][8][9][10] [11][12].

Amongst the rare earth based materials, oxy sulfides are rapidly achieving technological importance. They are an excellent laboratory system for the systematic investigation of rare-earth luminescence because almost all rare earth activators exhibit high luminescent efficiency and possess the same crystallographic structure regardless of ion size[13]. Lanthanum Oxysulfide is uniaxial p$\bar{3}$m crystal (hexagonal) and wide indirect bandgap (4.6ev – 4.8ev) semiconductor material [14] [15]. This wide-bandgap enables to minimize the phonon emission, which is a favourable condition for Photoluminescence [16]. Lanthanum oxysulfide has high thermal as

well as chemical stability. This gives it applicability in scientific and industrial field like steel industries [17][18][21], Catalysis [22][32], Ceramic industries [25], LASER [26], Electroluminescent [31] & Photoconductive [33] materials. Bi: La_2O_2S is used as cathodoluminescent material [19]. Eu^{3+}: La_2O_2S is used in surface temperature imaging [30], non-contact optical temperature sensor [20] [24] and as scintillator in optical fiber sensor for detecting Ultraviolet radiation in real-time [34]. Tb^{3+}: La_2O_2S is used as optical sensor for human skin temperature measurement [27] & in X-ray imaging [29].

Lanthanum Oxysulfide is synthesized by different methods. These include Solid State reaction in which first nitrate converted into Oxalate then Oxalate decomposed into oxy sulfide [54][53][45], Sulfur – Carbonate flux method [52], Rose's mixture flux technique [48], by passing H_2 gas at high temperature [51][44][41], using sulfurization agent in melt of alkali metal salts [50], Catalyst Technique [49][30], Gel thermolysis [47], combustion reaction with dithiooxamide as fuel [46], Two step method where combustion is followed by solid state technique [28], Solid State reaction with sulfurization flux (Na_2CO_3 & S powder) [43], Precipitation method [42][25], two step method involving hydrothermal and solid state method [40] by passage of N_2 / H_2 gas mixture [55], Solid State flux method [39], reflux method [38], Solid State reaction in H_2S / N_2 gas atmosphere, Solid State reaction by passing CS_2 / CO gas in material which is pre synthesized by hydrothermal method [23], thermal decomposition in eutectic molten salt [36], One step flux method [35] and ethanol assisted combustion technique [18][37].

As discussed above, three different techniques were used to synthesized Lanthanum oxysulfide. First by solid-state reaction, second by hydrothermal reaction and third by furnace combustion technique. The approach was to limit the amount of precursors to minimize the use of resources.

This method doesn't need the use of H_2S, CS_2, or any hazardous gases during the reaction. This method gives good yield in less time and hence has good scope to become industrial friendly technique.

The analysis of structural parameters from XRD suggests that the furnace combustion technique is the best technique to synthesized Lanthanum oxysulfide. In this technique, Lanthanum Nitrate Hexahydrate and Thioure (an organosulfur compound) is used as precursors with urea – ethanol as fuel. No pre or post-treatment is required. It gives high yield in less time. This technique is briefly described in the experimental as well as in result & analysis sections. The technique is different from the previous ethanol combustion technique. In the previous method, thioacetamide was used as a precursor and pre or post-treatment was required for completing the production.

As mentioned above, four samples of down conversion 1%Pr^{3+}: La_2O_2S, 1%Eu^{3+}: La_2O_2S, 1%Tb^{3+}: La_2O_2S, 1%Dy^{3+}: La_2O_2S and six samples of upconversion 4%Yb^{3+}-1%Er^{3+}: La_2O_2S, 12%Yb^{3+}-2%Er^{3+}: La_2O_2S, 4%Yb^{3+}-1%Ho^{3+}: La_2O_2S, 12%Yb^{3+}-2%Ho^{3+}: La_2O_2S, 4%Yb^{3+}-1%Tm^{3+}: La_2O_2S, 12%Yb^{3+}-2%Tm^{3+}: La_2O_2S were synthesized by furnace combustion technique.

To the best of our knowledge, this is the first work to report this kind of industrial friendly, furnace combustion technique for the synthesis of Lanthanum oxysulfide.

4.2 Experimental Procedure:

As mentioned above, three techniques were used to synthesize the pristine Lanthanum oxysulfide.

Two samples were synthesized by Solid State method. The precursor for the first sample was

Lanthanum nitrate hexahydrate (La $(NO3)_3.6H_2O$) and thiourea (NH_2CSNH_2). The mixture of these materials in stoichiometric proportion was poured in the crucible and kept in the furnace at 1000°C for 8 hours. For the second sample same precursors were used along with the addition of flux. Sulfur powder used as a flux. The mixture was kept in the furnace for 8 hours at 1000°C. After the reaction, both the samples were allowed to cool down naturally. They were in porous form. The samples were crushed into fine powder by using a mortar pestle.

Two samples were synthesized by hydrothermal method. The precursors for the first sample were Lanthanum nitrate hexahydrate ($La(NO3)_3.6H_2O$) and thiourea (NH_2CSNH_2). The mixture of these materials in stoichiometric proportion was dissolved in 100ml water and stirred for 5 minutes, then poured in an autoclave and kept at 250°C for 24 hours. The same method with same precursors were used for the second sample but with added flux (sulfur powder). Products were filtered and washed by deionized water and dried at 150°C for 2 hours in oven.

Two samples were synthesized by Furnace Combustion Method. For the first sample, stoichiometric amounts of Lanthanum nitrate hexahydrate ($La(NO3)_3.6H_2O$) and thiourea (NH_2CSNH_2) were taken. 2 gm of Urea as fuel, 5 ml ethanol and 10 ml deionized water were added to get a mixture, which was poured in a crucible and kept in the furnace. The same precursor and method were used for the second sample with addition of flux (sulfur powder). The combustion started on a full scale at 490°C in about 20 minutes and a massive amount of fumes were released. The furnace was shut down and products were allowed to cool down naturally in the furnace. After 24 hours, the crucibles were taken out from the furnace. The product was crushed in fine powder form by using a mortar – pestle. A high amount of yield was obtained.

The XRD characterization of samples showed better results for the Furnace combustion technique in both cases i.e. with and without flux. It is discussed in the results and analysis section. As the XRD results were similar in both cases, it was better to go for a simpler technique by limiting the use of precursors. Hence, furnace combustion technique without flux was used to synthesize rare earth elements doped Lanthanum oxysulfide. For ready reference, the four samples of downconversion and six compounds of upconversion are once again listed below.

Down conversion

1% Pr^{3+}: La_2O_2S 1% Eu^{3+}: La_2O_2S 1% Tb^{3+}: La_2O_2S 1% Dy^{3+}: La_2O_2S

Up conversion

4%Yb^{3+}-1%Er^{3+}: La_2O_2S 12%Yb^{3+}-2%Er^{3+}: La_2O_2S 4%Yb^{3+}-1%Ho^{3+}: La_2O_2S

12%Yb^{3+}-2%Ho^{3+}: La_2O_2S 4%Yb^{3+}-1%Tm^{3+}: La_2O_2S 12%Yb^{3+}-2%Tm^{3+}: La_2O_2S

4.3 Results and Analysis of Down conversion samples:

4.3.1 Structural and Elemental analysis:

A Bruker X-ray diffractometer with Cu Kα radiation with 2θ interval between 5°-75° degrees was used for the study of phase and structural characterization of pristine La_2O_2S as well as all doped La_2O_2S materials.

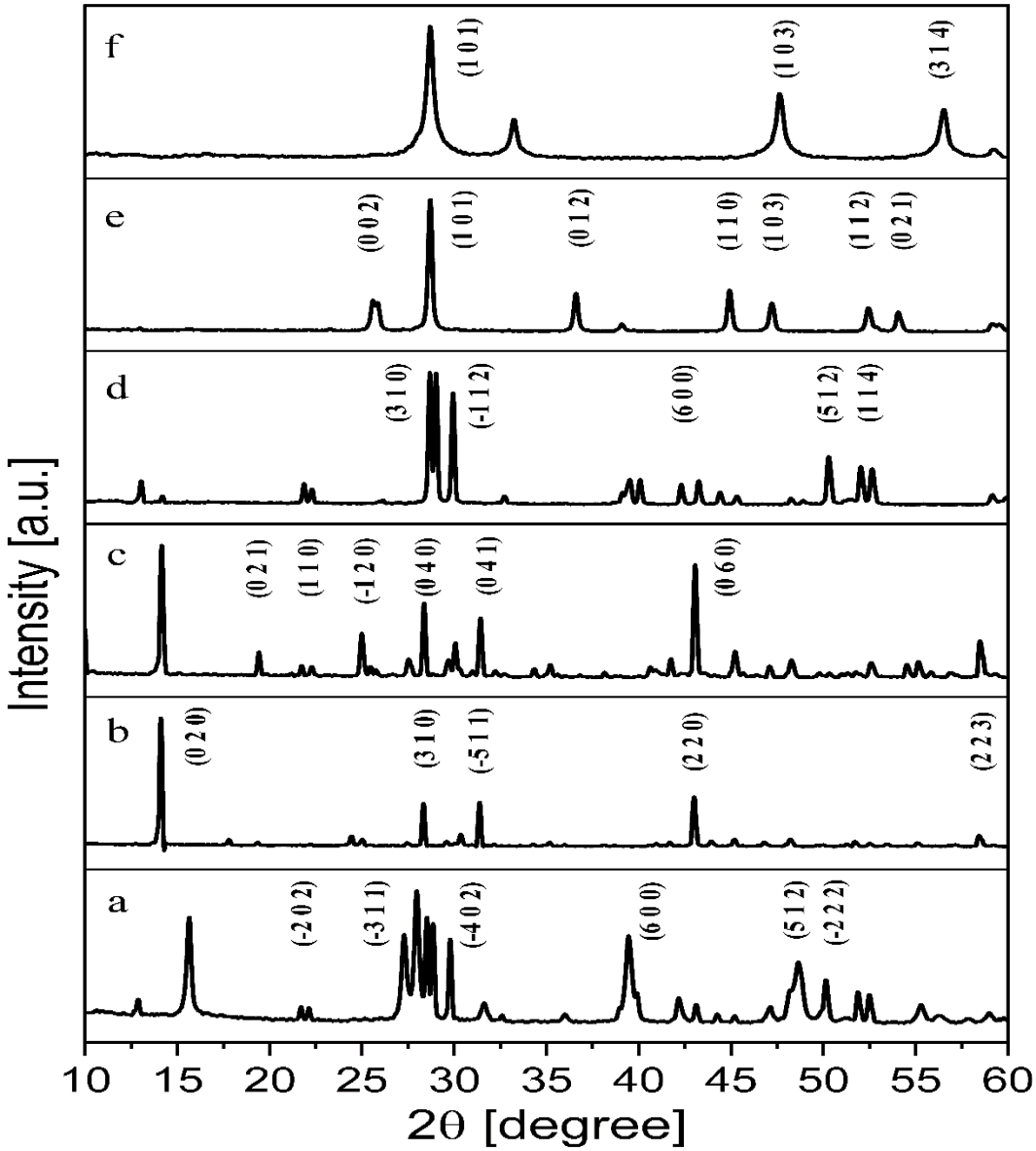

Figure 4.1 (a) XRD pattern of material synthesized by the solid-state method without flux

(b) XRD pattern for a solid-state method with flux

(c) XRD pattern of a hydrothermal method without flux

(d) XRD pattern for a hydrothermal method with flux

(e) XRD pattern for the combustion method without flux

(f) XRD pattern for the combustion method with flux

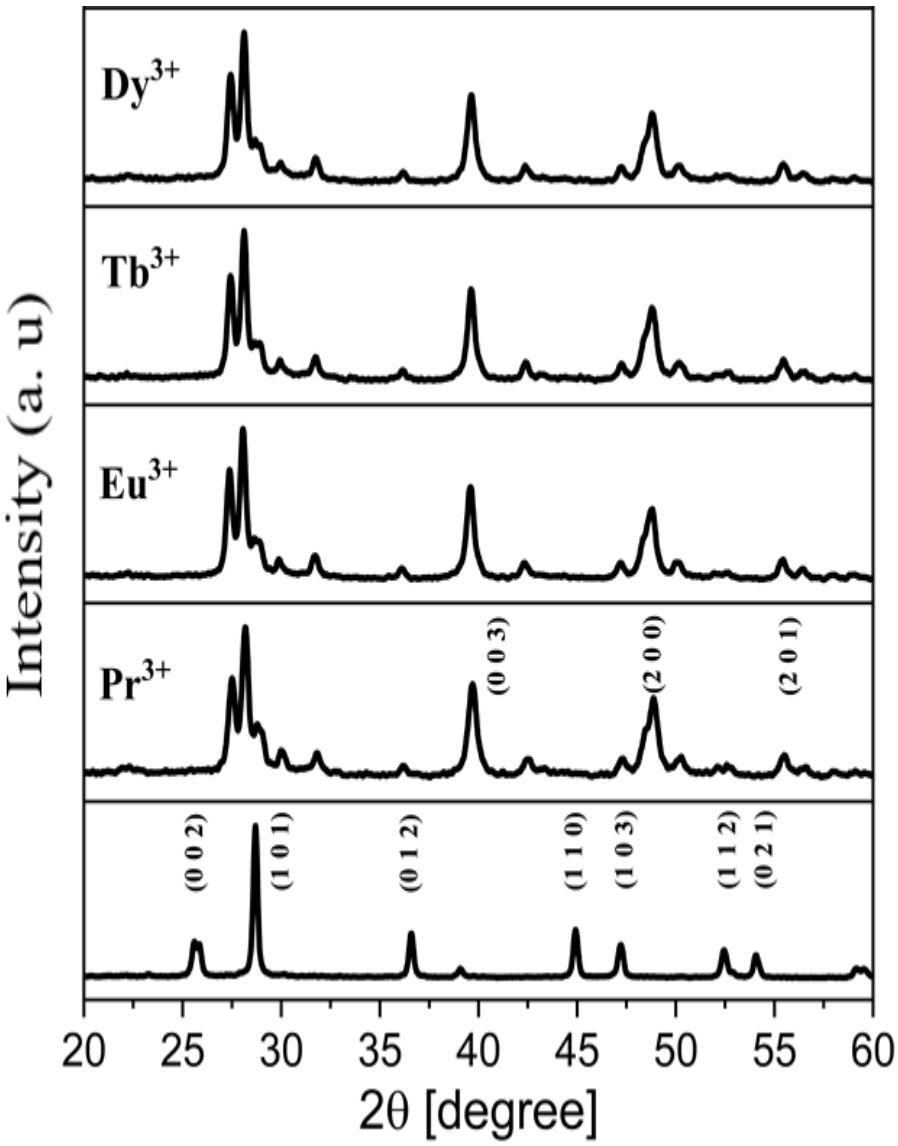

Figure 4.2 XRD pattern of pristine La_2O_2S and 1%Ln^{3+}: La_2O_2S

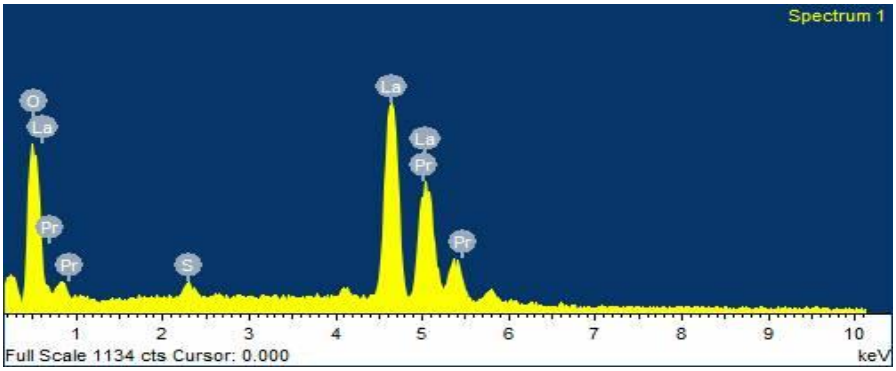

Figure 4.3 (a) EDAX spectrum of 1%Pr^{3+}: La_2O_2S

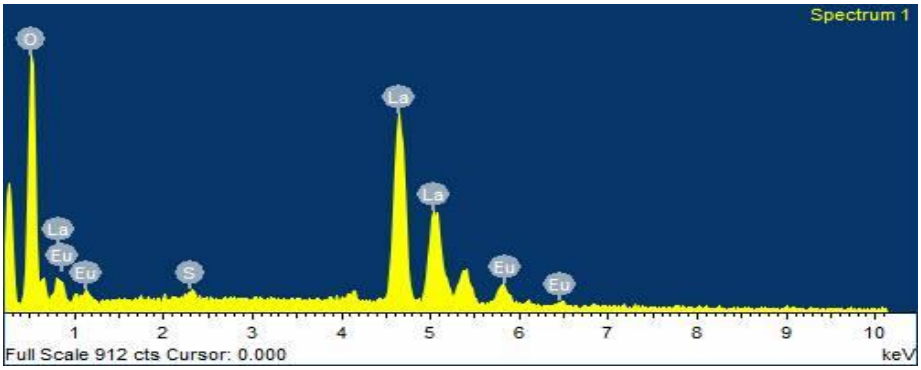

Figure 4.3 (b) EDAX spectrum of 1%Eu^{3+}: La_2O_2S

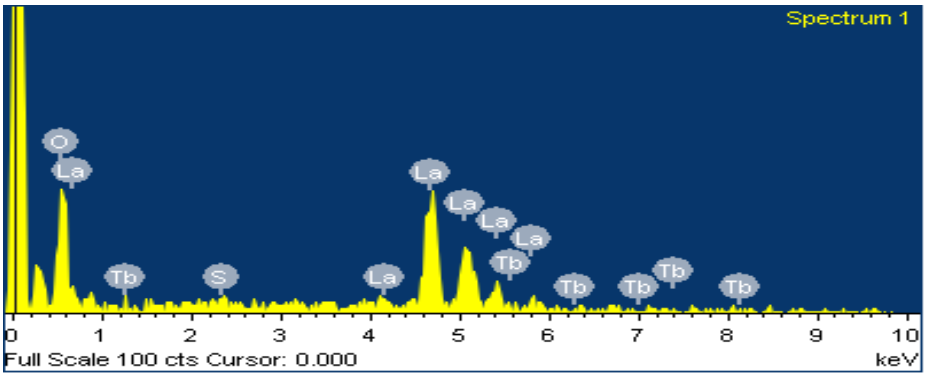

Figure 4.3 (c) EDAX spectrum of 1%Tb^{3+}: La_2O_2S

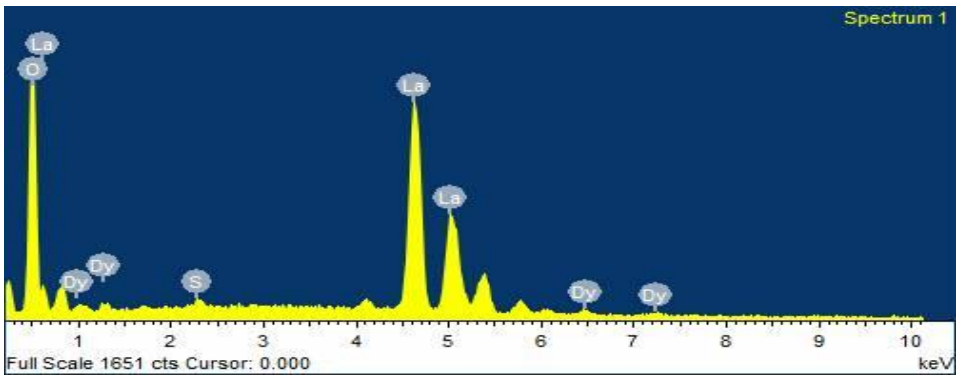

Figure 4.3 (d) EDAX spectrum of 1%Dy^{3+}: La_2O_2S

Synthesis Methods	Phase Name with space group	ICDD	Avg. Crystallite Size (nm)	Density (g/cm^3)	Volume ($A^{\circ 3}$)
Solid State					
Without Flux	La_2O_6S(15:C12/C1) Oxolanthanum sulfate	085-1535	52.21	5.466	493.21
With flux 1%	La_2O_6S(15:C12/C1) Oxolanthanum sulfate	085-1535	68.38	5.532	487.34
Hydrothermal					
Without flux	$La(OH)SO_4$(14:P121/n1) Lanthanum hydroxide sulfate	073-5330	84.87	4.37	484.33
1%flux	La_2O_6S(15:C12/C1) Oxolanthanum sulfate	085-1535	74.58	5.56	382.36
Furnace combustion					
Without flux	La_2O_2S(164:P-3m1) Lanthanum oxysulfide	075-1930	31.9	5.83	97.28
1%flux	La_2O_2S(164:P-3m1) Lanthanum oxysulfide	071-2098	30.7	5.83	97.25

Table 4.1 Structural data from the XRD spectra of three different synthesis routes

Materials	Phase Name	JCPDS no.	Avg. Crystallite Size (nm)	Volume ($A^{\circ 3}$)
La_2O_2S	164:P-3m1	75-1930	31.9	97.28
Pr^{3+} : La_2O_2S	164:P-3m1	75-1930,	13.2	84.33
Eu^{3+} : La_2O_2S		75-1954,	19.5	
Tb^{3+} : La_2O_2S		27-0263 &	22.1	
Dy^{3+} : La_2O_2S		71-2098	18.2	

Table 4.2 Structural data of doped La_2O_2S extracted from the XRD spectra

Compound	Elements (Atomic %)						
	La	**S**	**O**	**Pr**	**Eu**	**Tb**	**Dy**
$La_2O_2S : Pr^{3+}$	38	19	39.5	2.5	-	-	-
$La_2O_2S : Eu^{3+}$	40.3	18.5	39.5	-	1.7	-	-
$La_2O_2S : Tb^{3+}$	39.66	19.65	38.55	-	-	2.14	-
$La_2O_2S : Dy^{3+}$	40.66	19.65	37.55	-	-	-	2.14

Table 4.3 EDAX data of 1%Ln^{3+}: La_2O_2S from the spectrum with Atomic percentage

Fig 4.1 shows the XRD pattern of all six samples synthesized by different techniques to obtain the desired pristine La_2O_2S. The structural and lattice data from the XRD pattern (fig. 4.1) are given in table 4.1. It is clear from the table that the solid-state and hydrothermal techniques, with flux and without flux, did not give the single-phase La_2O_2S. By solid-state technique with and without flux, the synthesized phase was bis oxolanthanum sulfate. Peaks were matched with ICDD/JCPDS file no. 85-1535 for the space group of monoclinic lattice. By the hydrothermal technique without flux, the phase obtained was lanthanum hydroxide sulfate. All peaks matched with JCPDS file no. 73-5330. The hydroxide was removed on the addition of flux in precursors and the phase was again stabilized as bis oxolanthanum sulfate.

In the furnace combustion technique with and without flux, a single phase hexagonal lattice with a highly crystalline structure was obtained. All peaks matched with JCPDS file no. 75-1930 for the sample without flux. For the sample with flux of sulfur powder, all peaks matched with JCPDS file no. 71-2098. The highest intensity peaks in both cases were observed at a 2θ value of 28.90° with hkl plane (1 0 1). The lattice parameters for the sample prepared using furnace combustion technique without flux are, a (A°) = b (A°) = 4.0344 & c (A°) = 6.9016 (ICDD file number 75-1930) and for with flux the lattice parameters are, a (A°) = b (A°) = 4.0313 & c (A°) =6.9097 (ICDD file number 71-2098). As can be seen from the XRD pattern for the furnace combustion method in fig. 4.1, the number of peaks decrease for the samples with flux. However, broadening in peaks is observed in sample with flux. Thus, it was confirmed that the furnace combustion technique with flux and without flux was a more appropriate technique for the synthesis of a hexagonal lattice of lanthanum oxysulfide. Hence, the furnace combustion technique without flux was selected for synthesis of samples.

Fig 4.2 shows the XRD pattern of doped La_2O_2S samples. The XRD pattern of the pristine

La_2O_2S is also given for ready reference. There are variations in the peaks of doped La_2O_2S samples. The number of peaks increased compared to pristine La_2O_2S, which indicates the presence of rare-earth ions in the host. The pattern of all the doped La_2O_2S samples were found to be the same. Almost all peaks of doped La_2O_2S show broadening in comparison to the peaks of pristine La_2O_2S. The first peak at 2θ value of 12.104° was matched with ICDD file number 27-0263, four peaks at 2θ values of 28.35°, 36.20°, 39.72°, and 52.25° were matched with ICDD file number 75-1930, three peaks at 2θ values of 27.54°, 48.93° & 55.43° were matched with ICDD file number 75-1954 and one peak at 2θ value of 47.31° was matched with ICDD file number 71-2098. All these files were of the single hexagonal lattice. The highest peak at 2θ value of 28°35' with the hkl plane (1 0 1) was the same as compared with the highest intensity peak of pristine La_2O_2S. Table no. 4.2 presents the structural data of doped La_2O_2S extracted from the XRD and its comparison with pristine La_2O_2S. From the table, the crystallite size and volume of the unit cell are seen to be decreasing in comparison to pristine sample. The pattern of the atomic radius is La>Pr>Eu>Tb>Dy. So all rare-earth dopant elements have an ionic radius less than the host element Lanthanum. This is the likely reason behind the decrease in crystallite size and volume of the unit cell. It can also cause shift of peaks in the XRD pattern as compared to those of pristine sample. If dopant size is smaller than the base metal, it occupies the interstitial position leading to strain in the lattice structure. d spacing between the atoms become less, which results in an increase in the peaks of XRD at a higher order of 2θ values, as can be seen from figure 4.2. Hence, the number of peaks increased at a higher value of 2θ on the right side of the spectrum. For the calculation of lattice parameters, all peaks were compared with standard hkl values. Here the values of lattice parameters were calculated from the peaks, and the values were a (A°) = b (A°) = 3.73 & c (A°) = 7.40. Fig. 4.4 shows the EDAX spectrum of La_2O_2S and 1% Ln^{3+}:

La_2O_2S. The spectrum shows traces of all lanthanide ions doped into the Lanthanum oxy sulfide and also identifies the elemental composition of the material. Table 4.3 shows the data extracted from the EDAX spectrum with an atomic percentage in composition.

4.3.2 UV – Visible analysis:

Shimadzu spectrometer was used for studying UV-Visible characteristics of pristine La_2O_2S as well as doped samples of 1%Ln^{3+}: La_2O_2S.

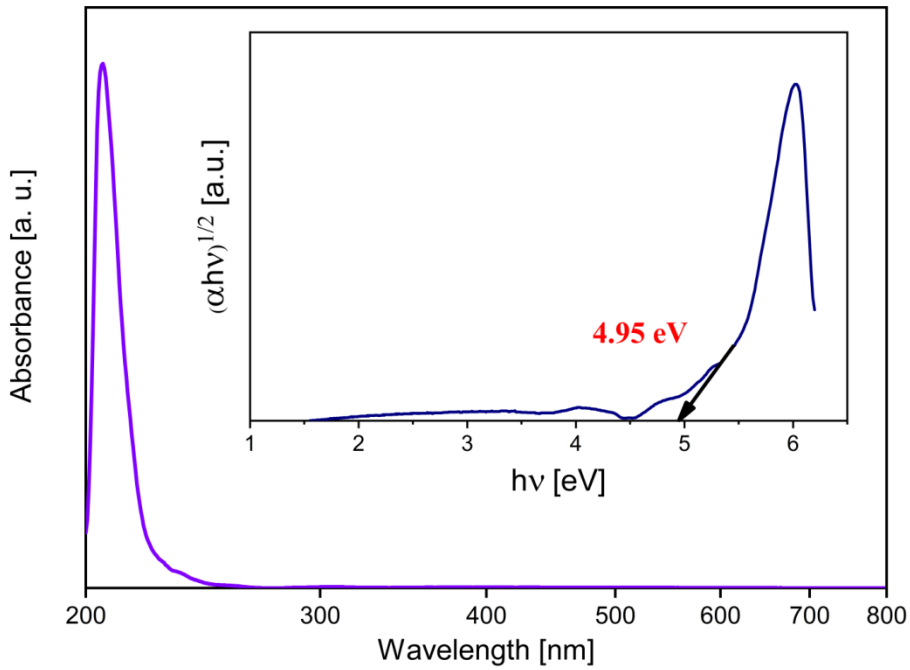

Figure 4.4 UV-Visible and Tauc's Plot of pristine La_2O_2S

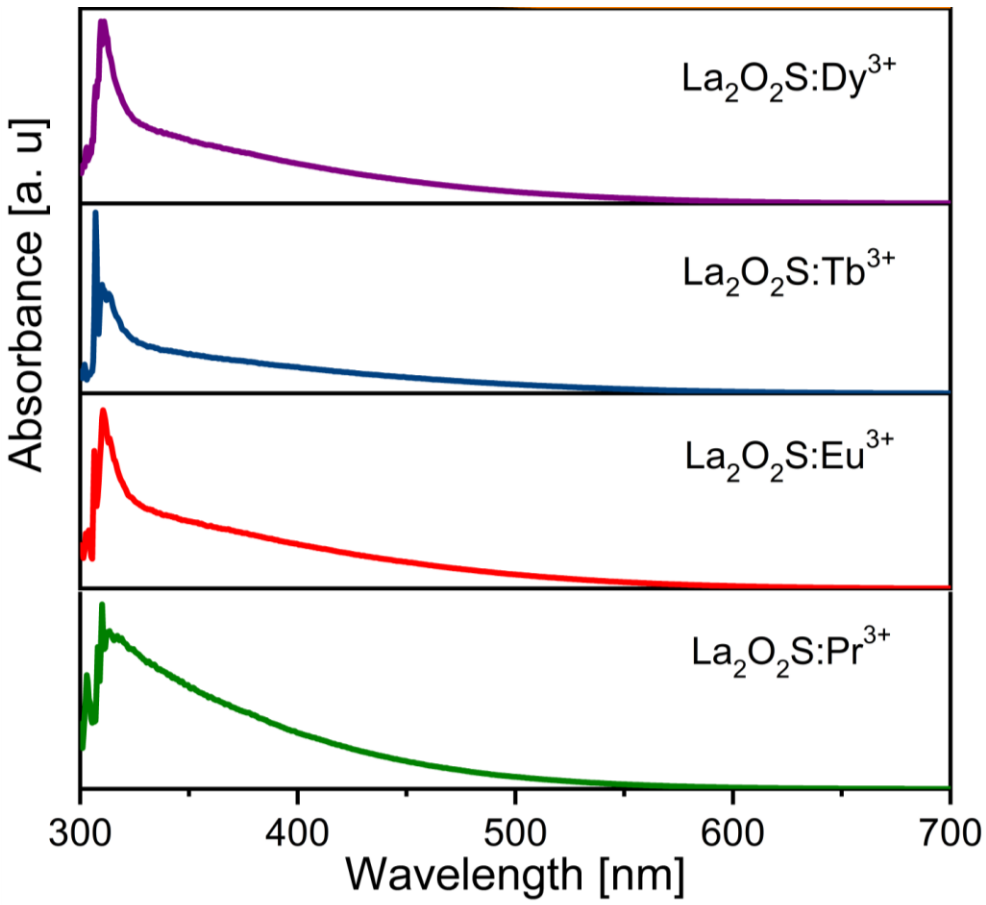

Figure 4.5 UV-Visible and Tauc's Plot of pristine La_2O_2S

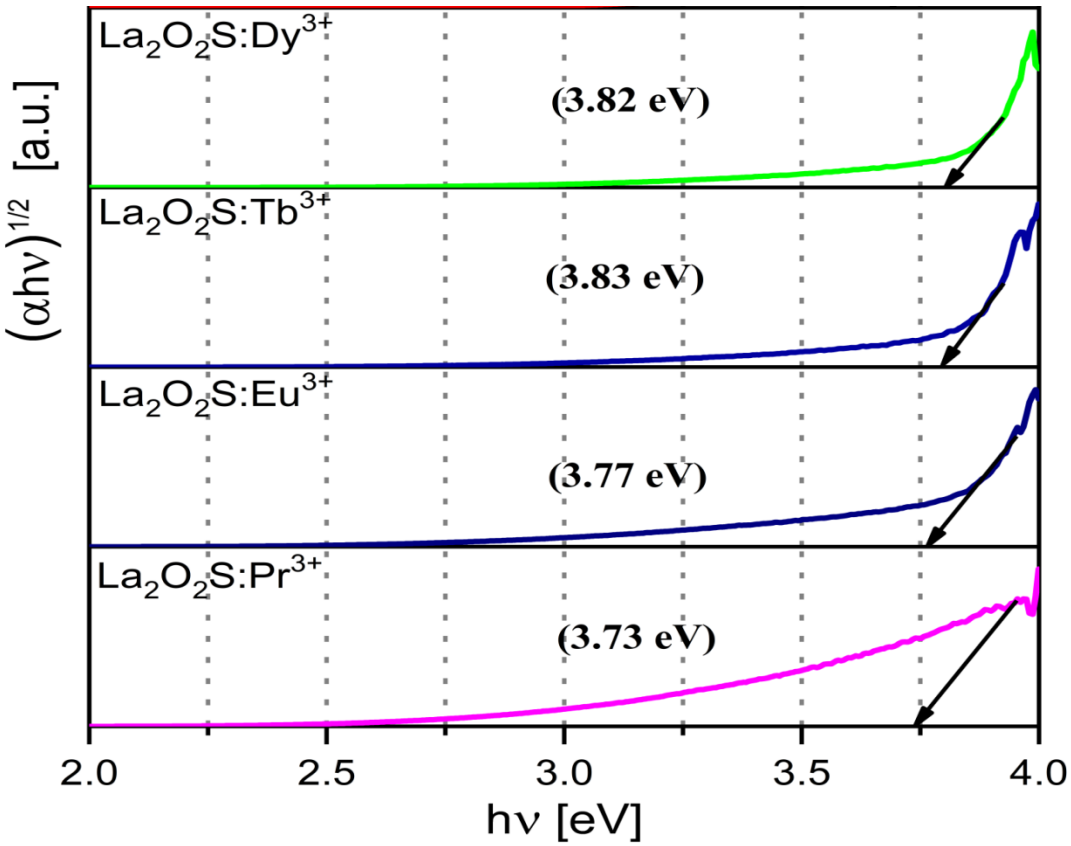

Figure 4.6 Tauc's plot of Ln^{3+}: La_2O_2S

Compounds	λ_{max} (nm)	Band Gap (eV)	Refractive index η	ε_λ Molar decadic extinction coefficient mol^{-1} cm^{-1}
La_2O_2S	208	4.95	2.00	20
$La_2O_2S : Pr^{3+}$	311	3.73	2.20	21
$La_2O_2S : Eu^{3+}$	313	3.77	2.19	31
$La_2O_2S : Tb^{3+}$	307	3.83	2.18	32
$La_2O_2S : Dy^{3+}$	313	3.82	2.20	27

Table 4.4 UV / VIS data of host La_2O_2S as well as 1%Ln^{3+}: La_2O_2S

Fig 4.4 shows the absorbance characteristics of pristine La_2O_2S and the Tauc's plot for the same, while Fig 4.5 shows the absorbance characteristics of four doped 1%Ln^{3+}: La_2O_2S samples. A 0.05 M solution was used for UV – Visible analysis of pristine La_2O_2S & Ln^{3+}: La_2O_2S. All the samples were dispersed in water media. Fig 4.6 shows the Tauc's plot for the estimation of optical band gap of the samples. Table 4.4 gives the data of the wavelength at which maximum absorbance is recorded along with the calculated Optical bandgap [56], refractive index [57] and molar extinction coefficient. The maximum absorbance of La_2O_2S is at the wavelength of 208 nm and the maximum absorbance of 1%Ln^{3+}: La_2O_2S samples is in wavelength range of 307 nm to 313 nm. Thus, there is a significant difference in absorbance maximum between La_2O_2S and 1%Ln^{3+}: La_2O_2S. The possible reason for this significant difference is that there is a predominant absorption between 2p orbital of O^{-2} to 4f orbital of Ln^{3+} [40][19]. Here the spectra is recorded for only one concentration value. If a series of concentrations can be used, the results would be interesting.

For the calculation of optical band gap, Tauc's plot based on the equation given below was used [56].

$$\alpha h\nu = K_1 (h\nu - E_g)^n \qquad (1)$$

This equation gives the relation between absorption coefficient α and the optical energy band gap E_g. The graph plotted between $(\alpha h\nu)^{1/n} \rightarrow (h\nu)$ is used to obtain the value of optical band gap. Here n = 2 taken for the allowed indirect electronic transition. The bandgap of pristine La_2O_2S was found to be 4.96 eV, which decreased in Ln^{3+}: La_2O_2S. The optical band gap was 3.73 eV for 1%Pr^{3+}: La_2O_2S, 3.77 eV for 1%Eu^{3+}: La_2O_2S, 3.83 eV for 1%Tb^{3+}: La_2O_2S, 3.82 eV for 1%Dy^{3+}: La_2O_2S. The overlapping of wave functions of electrons bound to the Ln^{3+}dopant

ions leads to the formation of an energy band, which might be a possible reason for decrease in the optical bandgap of doped samples.

The refractive index η was calculated from the equation given by V. Kumar and J. K. Singh [57].

$$\eta = K\, E_g^{c} \qquad (2)$$

Where, K = 3.3668 & C = -0.32234 are constant & E_g is the optical band gap.

The refractive index η was found to be 2.00 for La_2O_2S but varied between 2.18 to 2.20 for Ln^{3+}: La_2O_2S samples.

The molar extinction coefficient was calculated from the Beer – Lambert law using the equation

$$\varepsilon = \frac{A}{LC} \qquad (3)$$

Here A is the amount of light absorbed by the sample for a particular wavelength, L is the distance that the light travels through the solution and C is the concentration of the absorbing species per unit volume.

4.3.3 Photoluminescence analysis:

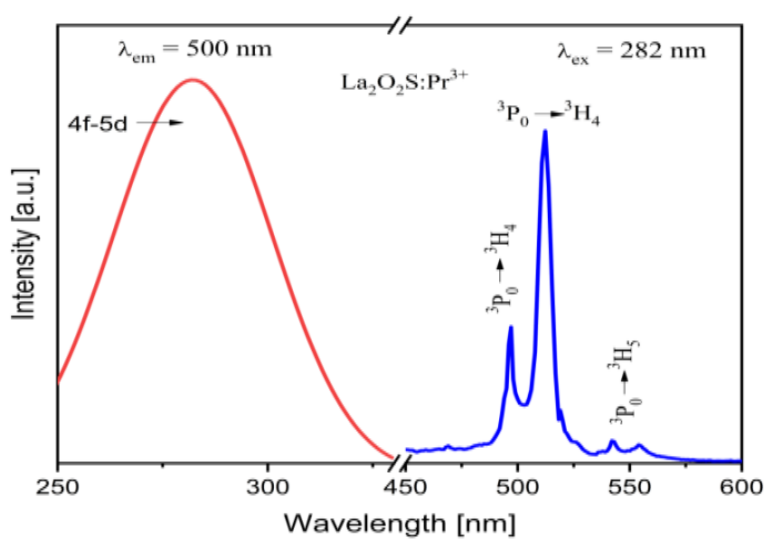

Figure 4.7(a) emission and excitation graph of doped 1%Pr^{3+}: La_2O_2S

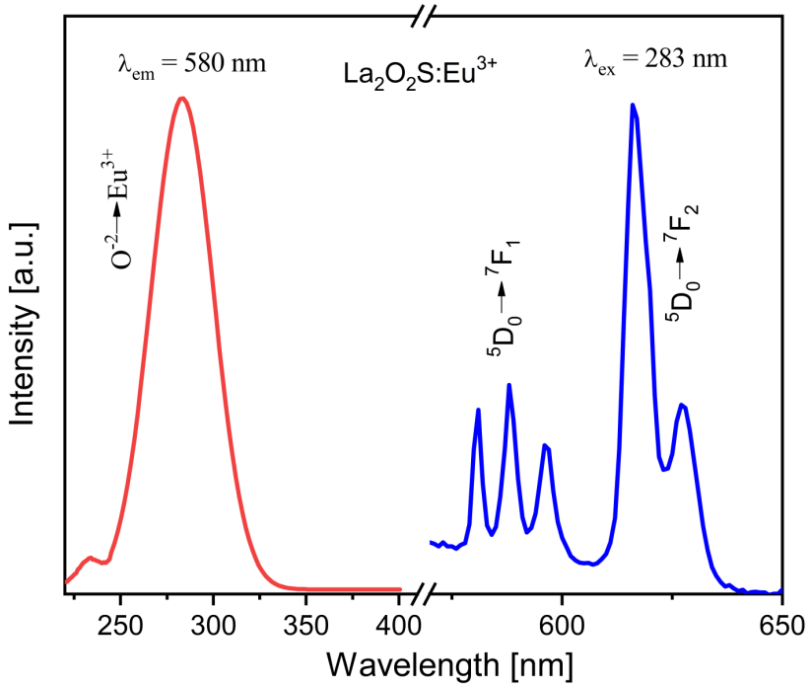

Figure 4.7(b) emission and excitation graph of doped 1%Eu^{3+}: La_2O_2S

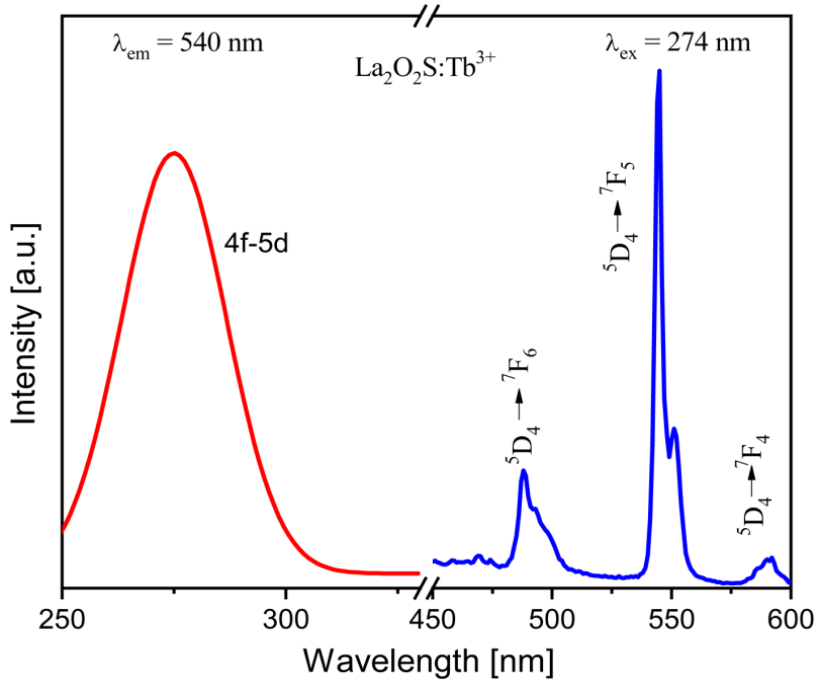

Figure 4.7(c) emission and excitation graph of doped 1%Tb^{3+}: La_2O_2S

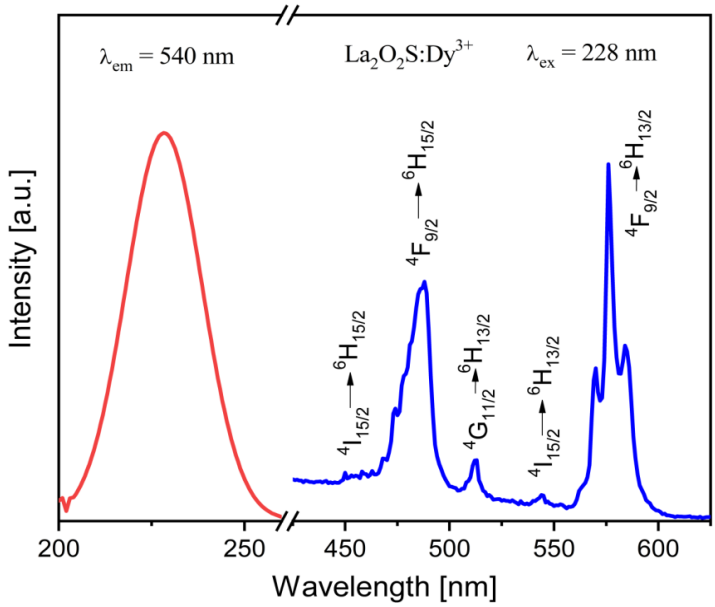

Figure 4.7(d) emission and excitation graph of doped 1%Dy^{3+}: La_2O_2S

The PL excitation and emission spectra of Pr^{3+}: La_2O_2S is shown in fig. 4.7 (a). The $4f^2$ configuration of Pr^{3+} has 13 energy levels available for transitions [61]. The excitation spectrum was recorded at the emission wavelength of λ_{emi} 500 nm. The 4f5d transition in Pr^{3+}: La_2O_2S is responsible for the excitation band which has a maximum at wavelength of 282 nm [55][59][60]. The ground state energy level is $^3H_4$ and $^1S_0$ is the highest energy level at 48800 cm^{-1} for Pr^{3+}. The 4f5d transitions are observed at approximately 35460 cm^{-1}, which is lower than the highest excitation energy level of Pr^{3+}. The PL emission spectra was recorded at an excitation wavelength of λ_{exc} 282 nm. A sharp and intense peak is observed at 512 nm and another peak with lower intensity is observed at 498 nm. The transition from energy level $^3P_0$ (20474.93 cm^{-1}) to ground energy level $^3H_4$ is responsible for peaks at 498 nm and at 512 nm [61]. Two weaker peaks are observed at a wavelength of 541 nm and at a wavelength of 554 nm, which can be ascribed to the transition from energy level $^3P_0$ (20474.93 cm^{-1}) → $^3H_5$ (2222 cm^{-1}).

From the fig 4.7 (b) Eu^{3+}: La_2O_2S, the PL excitation maximum can be seen at 283 nm. The

monitoring emission wavelength is λ_{emi} = 580 nm. The CTS (charge transfer transition) is responsible for this, in which transition between 2p orbital of O^{2-} and 4f orbital of Eu^{3+} at 35460 cm^{-1} energy level occurs [19][40]. The Emission spectra was recorded at an excitation wavelength of λ_{exc} = 283 nm. There are five emission peaks at the wavelength of 581 nm, 587 nm, 596 nm, 616 nm and 626 nm. These are due to 4f-4f the transition. The transition between energy levels $^5D_0$ (17267 cm^{-1}) → $^7F_0$ (ground level) is responsible for the emission at a wavelength of 581 nm. The peaks at 587 nm and 596 nm are due to the transition $^5D_0 \rightarrow {}^7F_1$ (355 cm^{-1}). The emission at wavelengths of 616 nm and 626 nm are due to the transition between $^5D_0 \rightarrow {}^7F_2$ (1022 cm^{-1}) [61].

From fig 4.7 (c) for Tb^{3+}: La_2O_2S, the maximum excitation is observed at a wavelength of 274 nm for the emission wavelength λ_{emi} = 540 nm. The 4f5d transition is accountable for this excitation[35][55]. Under the excitation of 274 nm, three emission peaks are observed. The transition between $^5D_4$ (20462.60 cm^{-1}) $\rightarrow {}^7F_6$ (ground level) was responsible for emission peak at a wavelength of 487 nm. The transition between $^5D_4 \rightarrow {}^7F_5$ (2043.26 cm^{-1}) is responsible for the peak with highest intensity at 543 nm. The peak at 590 nm is due to $^5D_4 \rightarrow {}^7F_4$ (3266.42 cm^{-1}) [61].

In fig 4.7 (d) for Dy^{3+}: La_2O_2S, the excitation is recorded at an emission wavelength of 540 nm. The excitation is maximum at a wavelength of 228 nm. The host absorption is accountable for this excitation [58][59][60]. Under the excitation at a wavelength of 228 nm, there were six emission peaks spotted at wavelengths of 450 nm, 458 nm, 487 nm, 512 nm, 544 nm & 575 nm. The highest intensity peak is at 575 nm due to the $^4F_{9/2}$ (21097 cm^{-1}) → $^6H_{13/2}$ (3556 cm^{-1}). The transition from $^4I_{15/2}$ (22247 cm^{-1}) → $^6H_{13/2}$ is responsible for the peak at a wavelength of 544 nm, which is less intense. The two weak peaks observed at the wavelength of 450 nm and 458

nm are due to the transition of $^4I_{15/2} \rightarrow {}^6H_{15/2}$ (ground level). The second highest intense peak was spotted at wavelength 487 nm due to the transition of $^4F_{9/2} \rightarrow {}^6H_{15/2}$. The transition of $^4G_{11/2}$ (23215 cm^{-1}) $\rightarrow {}^6H_{13/2}$ is responsible for a peak at a wavelength of 512 nm [61].

4.4 Results and Analysis for upconversion samples:

4.4.1 Structural analysis:

A Bruker X-ray diffractometer with Cu Kα radiation was used for the study of phase, and structural characterization. The 2θ interval was taken between 5°-75°.

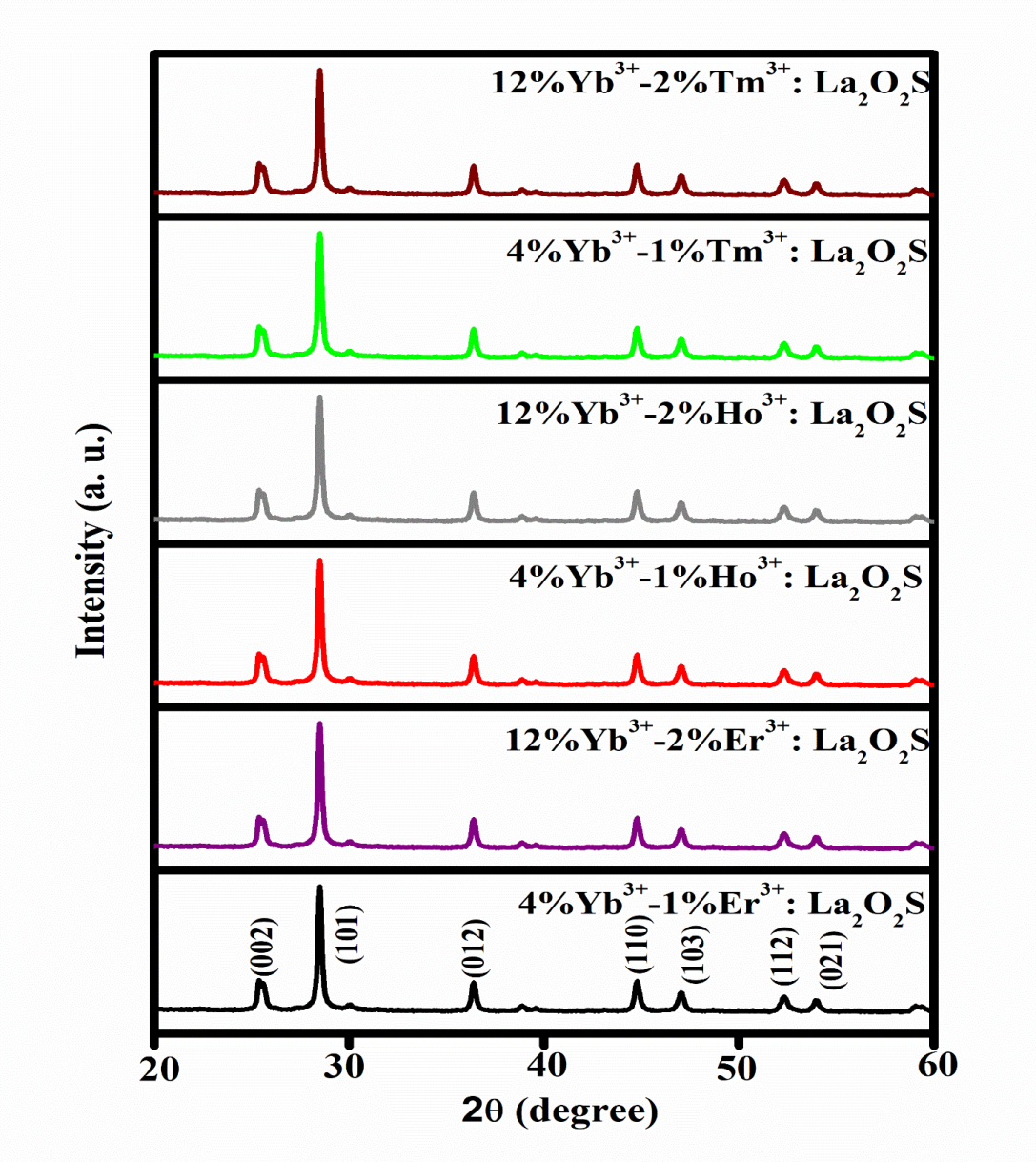

Figure 4.8 XRD of upconversion samples

Materials	Phase Name	JCPDS no.	Avg. Crystallite	Volume ($A^{\circ 3}$)

			Size (nm)	
4%Yb^{3+}-1%Er^{3+}: La_2O_2S			13.2	
12%Yb^{3+}-2%Er^{3+}: La_2O_2S			14.5	
4%Yb^{3+}-1%Ho^{3+}: La_2O_2S	164:P-3m1	75-1930, 75-1954, 27-0263, 71-2098	13.1	84.33
12%Yb^{3+}-2%Ho^{3+}: La_2O_2S			12.2	
4%Yb^{3+}-1%Tm^{3+}: La_2O_2S			12.9	
12%Yb^{3+}-2%Tm^{3+}: La_2O_2S			13.2	

Table 4.5 Structural data of doped La_2O_2S samples extracted from the XRD spectra

4.4.2 Photoluminescence analysis:

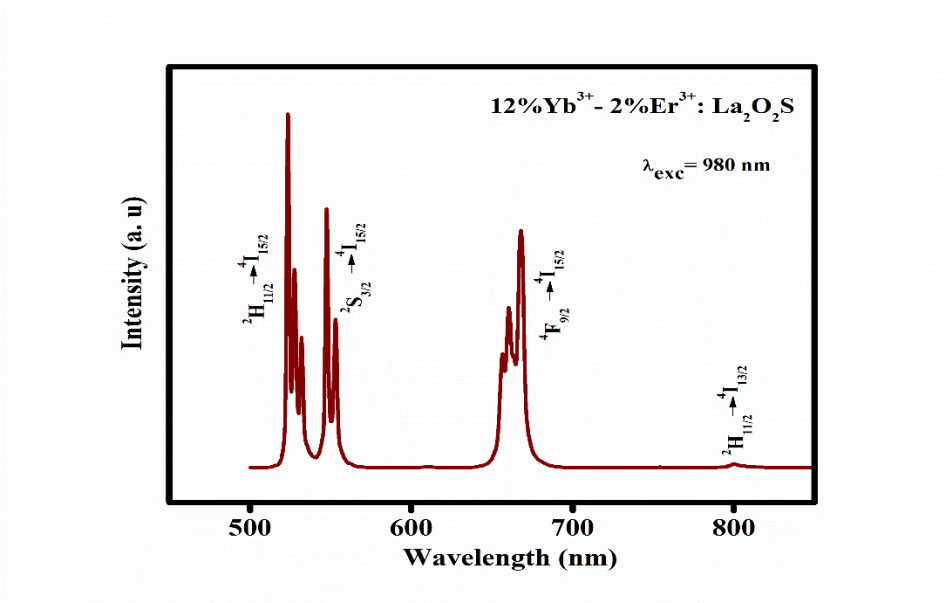

Figure 4.9 (a) Excitation & Emission characteristics of 12%Yb^{3+}-2%Er: La_2O_2S

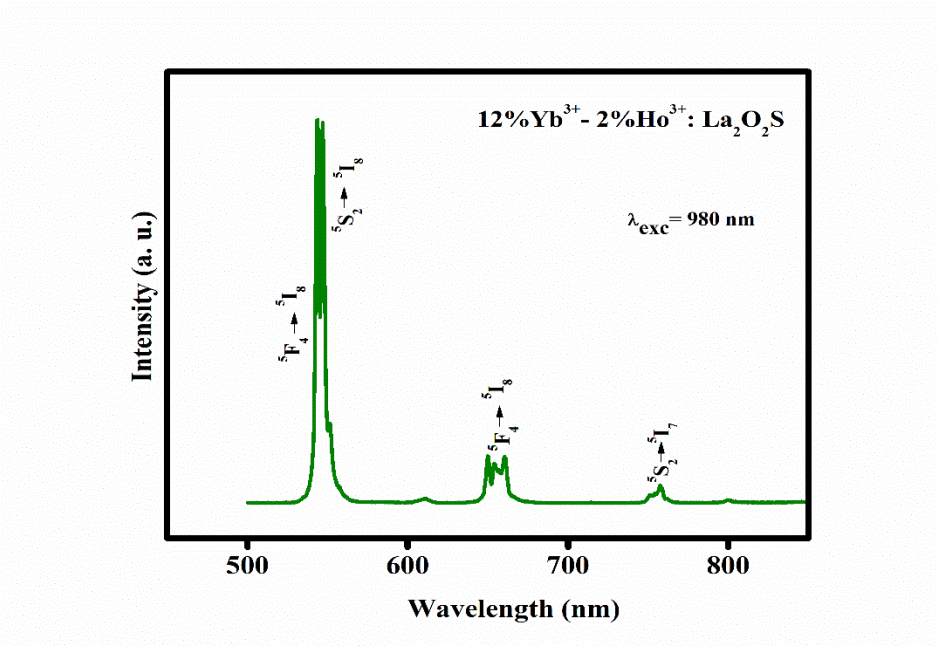

Figure 4.9 (b) Excitation & Emission characteristics of 12%Yb^{3+}-2%Ho: La_2O_2S

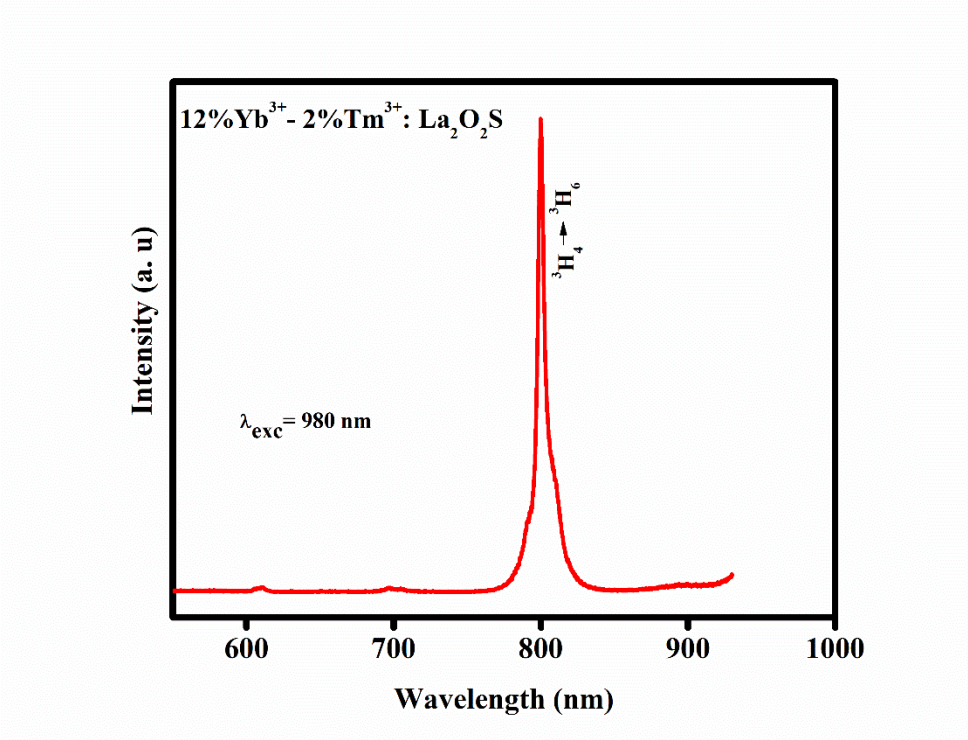

Figure 4.9 (c) Excitation & Emission characteristics of 12%Yb^{3+}-2%Tm: La_2O_3

Fig. 4.9 (a) shows the PL upconversion spectrum of 12%Yb^{3+}-2%Er: La_2O_2S under 980 nm excitation. Three major peaks were observed: $^2H_{11/2}\rightarrow{}^4I_{15/2}$, $^2S_{3/2}\rightarrow{}^4I_{15/2}$, $^4F_{9/2}\rightarrow{}^4I_{15/2}$ with maxima at 523 nm, 547 nm, and 668 nm, respectively and a minor peak at 800 nm attributed to $^2H_{11/2}\rightarrow{}^4I_{13/2}$ [61]. The Jablonski diagram clearly depicts the well-known mechanisms behind the PL. The Er^{3+} is solely capable of absorbing the 980 nm photons, as the upconversion is observed in single-doped materials. However, the absorption cross-section of Yb^{3+} at this wavelength is an order of magnitude greater. After Yb^{3+} gets excited to its only excited level, $^2F_{5/2}$, it non-radiatively transfers the energy to the nearest Er^{3+} ion. The most probable process for this transfer called energy transfer upconversion (ETU) or APTE (Addition of Photon for Transfer of Energy). The Er^{3+} has an optical center in $^4I_{11/2}$ level. It can radiatively de-excite NIR photons or it can experience the second boost to the higher levels, most probably by ETU. Two pathways are observed: (i) $^4I_{11/2}\rightarrow{}^4F_{7/2}$, or (ii) non-radiative de-excitation to $^4I_{11/2}$ with subsequent phonon-assisted upconversion to $^4F_{9/2}$. Once in $^4F_{7/2}$, Er^{3+} may experience multiphonon de-excitation in steps down to $^4F_{9/2}$, competing with the radiative emissions from each of the levels on this path. As the maximum phonon energy in La_2O_2S is 710 cm^{-1}, the multiphonon process is very probable for such small gaps [24].

Fig. 4.9 (b) displays the upconversion photoluminescence emission spectra of La_2O_2S: 12%Yb^{3+}-2% Ho^{3+} under 980 nm excitation. The major peak (green emission) originates from the electron transitions between closely spaced $^5F_4$ and $^5S_2$ levels and the $^5I_8$ ground level. The slightly weaker emission (red emission centered at 667 nm) is attributed to $^5F_5\rightarrow{}^5I_8$ transition and the emission of the lowest intensity peak is located around 760 nm and is due $^5S_2\rightarrow{}^5I_7$ transition [61].

PL spectra of the Tm^{3+} co-doped sample is given in Fig. 4.9 (c). The emission is due to the

$^3H_4 \rightarrow {}^3H_6$ transitions at 799 nm [61].

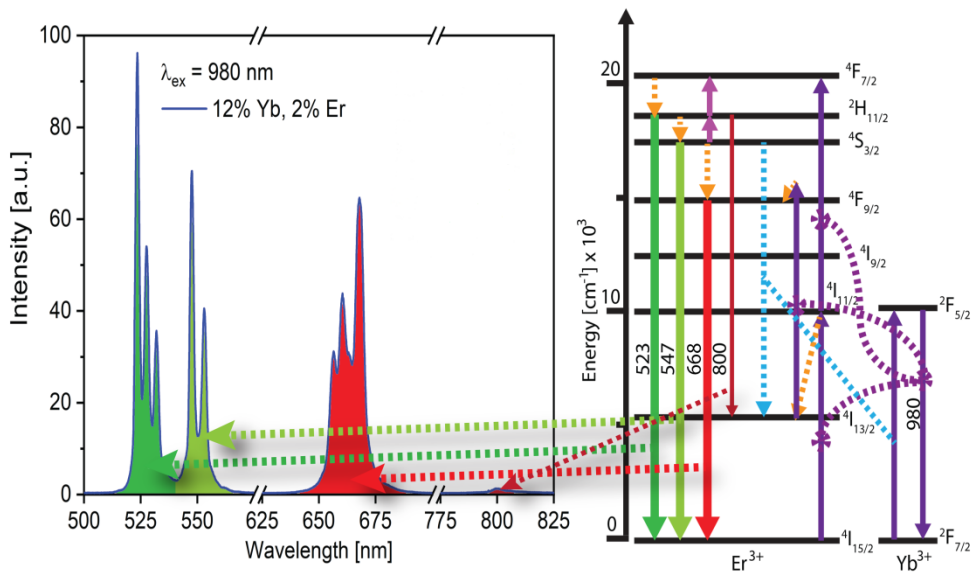

Figure 4.10 (a) Energy level diagram for Upconversion photoluminescence of 12%Yb^{3+}- 2%Er^{3+}: La_2O_2S

As shown in Fig. 4.10 (a), the excitation energy at 980 nm is absorbed by the Yb^{3+} as well as Er^{3+} ions. The Yb^{3+} ions and Er^{3+} ions have the same energy for the first excited state. The excitation results into transitions from $^2F_{7/2} \rightarrow {}^2F_{5/2}$ levels in Yb^{3+} ions and $^4I_{15/2} \rightarrow {}^4I_{11/2}$ levels in Er^{3+} ions. Thus both the ions undergo Ground State Absorption. The energy emitted by the Yb^{3+} ions while returning to the ground state is transferred to the Er^{3+} ions, due to which they are propelled to the higher energy levels as shown in the diagram. The decay from these higher energy levels to the ground state $^4I_{15/2}$ in Er^{3+} ions results in emissions.

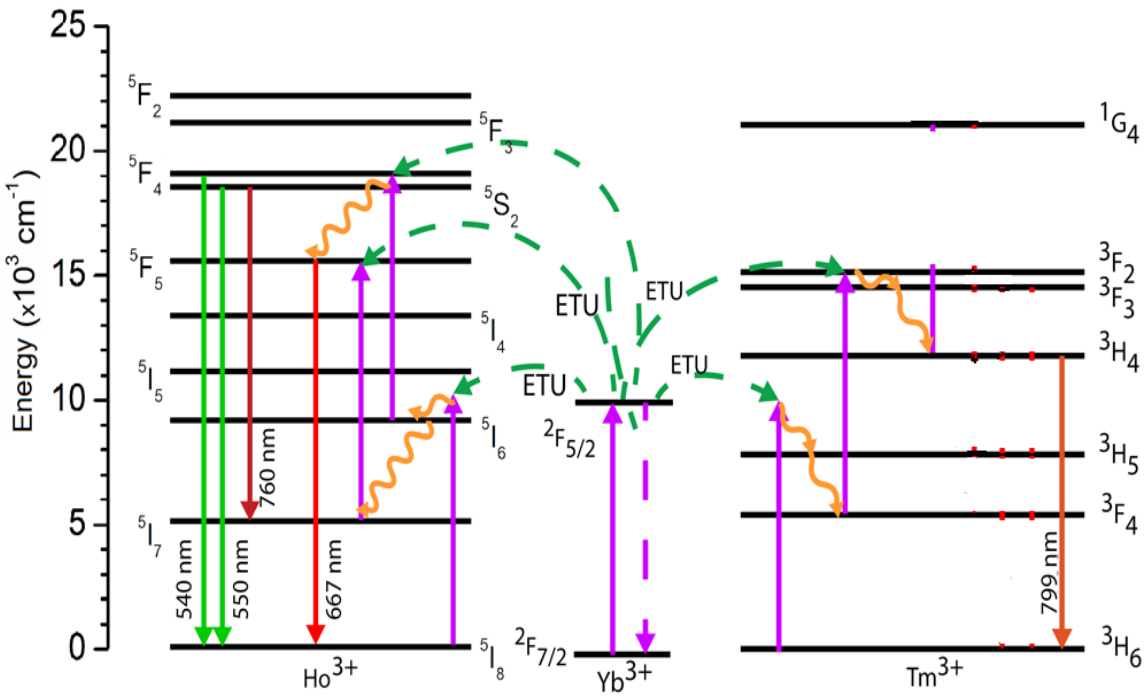

Figure 4.10 (b) Energy level diagram for Upconversion photoluminescence of 12%Yb^{3+}- 2%Ho^{3+}: La$_2$O$_2$S & 12%Yb^{3+}- 2%Tm^{3+}: La$_2$O$_2$S

As shown in fig 4.10 (b) for 12%Yb^{3+}- 2%Ho^{3+}: La$_2$O$_2$S, the excitation at 980 nm is absorbed by only Yb^{3+} ions. This ground state absorption results into the transition $^2F_{7/2}\rightarrow{}^2F_{5/2}$ and subsequent emission from $^2F_{5/2}\rightarrow{}^2F_{7/2}$. The emitted energy also triggers the ground state absorption of Ho^{3+} ions from $^5I_8$. The emitted energy from Yb^{3+} ions further excites the Ho^{3+} ions at $^5I_6$ to the higher energy levels. The decay from these higher energy levels to the ground state $^5I_8$ in Ho^{3+} ions results in emissions.

As shown in fig 4.10 (b) for 12%Yb^{3+}- 2%Tm^{3+}: La$_2$O$_2$S, the excitation at 980 nm is absorbed by only Yb^{3+} ions. This ground state absorption results into the transition $^2F_{7/2}\rightarrow{}^2F_{5/2}$ and subsequent emission from $^2F_{5/2}\rightarrow{}^2F_{7/2}$. The emitted energy triggers the ground state absorption of Tm^{3+} ions from $^3H_6$. The emitted energy from Yb^{3+} ions further excites the Tm^{3+} ions at $^3H_5$ to other excited states as shown in figure. The transition to the ground state $^3H_6$ of Tm^{3+} ions results

in emissions.

4.5 Conclusion:

From the comparative study of structural data obtained from the XRD spectra of the three synthesis techniques for the preparation of Lanthanum oxysulfide, the furnace combustion technique without sulfur powder as the flux was found to give the best results. It has the potential to become an industrial friendly technique as it requires less time for synthesis, less number of precursors and gives a perfect hexagonal lattice. Hence, the four down conversion and six upcoversion samples were synthesized by using the furnace combustion technique. All peaks were matched with ICDD files that confirmed the perfect hexagonal lattice. The host La_2O_2S had a optical bandgap of 4.96 eV which decreased significantly on doping. The refractive index and molar extinction coefficient were also calculated.

References:

[1] G.H. Dieke, R.A. Satten, Spectra and Energy Levels of Rare Earth Ions in Crystals, Am. J. Phys. (1970). doi:10.1119/1.1976350.

[2] A.R. Jha, Rare earth materials: Properties and applications, 2014. doi:10.1201/b17045.

[3] T. Wu, J. Zhou, B. Wu, W. Li, Effect of La2O3 content on wear resistance of alumina ceramics, J. Rare Earths. (2016). doi:10.1016/S1002-0721(16)60027-3.

[4] The rare earth elements: an introduction, Choice Rev. Online. (2016). doi:10.5860/choice.196797.

[5] W. Wu, F. Zhang, X. Bian, S. Xue, S. Yin, Q. Zheng, Effect of loaded organic phase containing mixtures of silicon and aluminum, single iron on extraction of lanthanum in saponification P507-HCl system, J. Rare Earths. (2013).

[6] C.H. Yan, Z.G. Yan, Y.P. Du, J. Shen, C. Zhang, W. Feng, Controlled Synthesis and

Properties of Rare Earth Nanomaterials, 2011. doi:10.1016/B978-0-444-53590-0.00004-2.

[7] Z.G. Yan, C.H. Yan, Controlled synthesis of rare earth nanostructures, J. Mater. Chem. (2008). doi:10.1039/b810586c.

[8] J. Shen, L.D. Sun, C.H. Yan, Luminescent rare earth nanomaterials for bioprobe applications, Dalt. Trans. (2008). doi:10.1039/b805306e.

[9] L. Yu, H. Song, S. Lu, Z. Liu, L. Yang, X. Kong, Luminescent properties of LaPO4:Eu nanoparticles and nanowires, J. Phys. Chem. B. (2004). doi:10.1021/jp047688c.

[10] G.C. Righini, M. Ferrari, Photoluminescence of rare-earth-doped glasses, Riv. Del Nuovo Cim. (2005). doi:10.1393/ncr/i2006-10010-8.

[11] C.D.S. Brites, P.P. Lima, N.J.O. Silva, A. Millán, V.S. Amaral, F. Palacio, L.D. Carlos, Organic-Inorganic Eu3+/Tb3+ codoped hybrid films for temperature mapping in integrated circuits, Front. Chem. (2013). doi:10.3389/fchem.2013.00009.

[12] A. Kitai, Luminescent Materials and Applications, 2008. doi:10.1002/9780470985687.

[13] L.E. Sobon, K.A. Wickersheim, R.A. Buchanan, R. V. Alves, Growth and properties of lanthanum oxysulfide crystals, J. Appl. Phys. (1971). doi:10.1063/1.1660682.

[14] C.W. Struck, W.H. Fonger, Dissociation of Eu+3 charge-transfer state in Y2O2S and La2O2S into Eu+2 and a free hole, Phys. Rev. B. (1971). doi:10.1103/PhysRevB.4.22.

[15] R. Vali, Electronic, dynamical, and dielectric properties of lanthanum oxysulfide, Comput. Mater. Sci. (2006). doi:10.1016/j.commatsci.2005.08.007.

[16] C. Koepke, A.J. Wojtowicz, A. Lempicki, Excited-state absorption in excimer-pumped CaWO4 crystals, J. Lumin. (1993). doi:10.1016/0022-2313(93)90003-6.

[17] C. Li, H. Wang, B. Bai, L. Zhang, Thermodynamic Analysis of Precipitation of La-O-S-As Inclusions in Steel, in: Miner. Met. Mater. Ser., 2019. doi:10.1007/978-3-030-05955-

2_75.

[18] Y. Hou, G. Xiong, L. Liu, G. Li, N. Moelans, M. Guo, Effects of LaAlO3 and La2O2S inclusions on the initialization of localized corrosion of pipeline steels in NaCl solution, Scr. Mater. (2020). doi:10.1016/j.scriptamat.2019.10.025.

[19] B.M. Jaffar, H.C. Swart, H.A.A. Seed Ahmed, A. Yousif, R.E. Kroon, Cathodoluminescence degradation of Bi doped La2O3 and La2O2S phosphor powders, Phys. B Condens. Matter. (2019). doi:10.1016/j.physb.2019.411659.

[20] L.J.B. Erasmus, H.C. Swart, J.J. Terblans, La2O2S:Eu3+ stability as temperature sensor, Appl. Surf. Sci. (2019). doi:10.1016/j.apsusc.2019.05.075.

[21] S. Imashuku, K. Wagatsuma, Cathodoluminescence Analysis of Nonmetallic Inclusions in Steel Deoxidized and Desulfurized by Rare-Earth Metals (La, Ce, Nd), Metall. Mater. Trans. B Process Metall. Mater. Process. Sci. (2020). doi:10.1007/s11663-019-01732-8.

[22] S. Tan, D. Li, Enhancing Oxygen Storage Capability and Catalytic Activity of Lanthanum Oxysulfide (La2O2S) Nanocatalysts by Sodium and Iron/Sodium Doping, ChemCatChem. (2018). doi:10.1002/cctc.201701117.

[23] Q. Pan, D. Yang, S. Kang, J. Qiu, G. Dong, Regulating Mid-infrared to Visible Fluorescence in Monodispersed Er3+-doped La2O2S (La2O2SO4) Nanocrystals by Phase Modulation, Sci. Rep. (2016). doi:10.1038/srep37141.

[24] G. Jiang, X. Wei, Y. Chen, C. Duan, M. Yin, B. Yang, W. Cao, Luminescent La2O2S:Eu3+ nanoparticles as non-contact optical temperature sensor in physiological temperature range, Mater. Lett. (2015). doi:10.1016/j.matlet.2014.12.057.

[25] J. Lian, B. Wang, P. Liang, F. Liu, X. Wang, Fabrication and luminescent properties of La2O 2S:Eu3+ translucent ceramic by pressureless reaction sintering, Opt. Mater. (Amst).

(2014). doi:10.1016/j.optmat.2014.01.024.

[26] I. Iparraguirre, J. Azkargorta, O. Merdrignac-Conanec, M. Al-Saleh, C. Chlique, X. Zhang, R. Balda, J. Fernández, Laser action in Nd^3+-doped lanthanum oxysulfide powders, Opt. Express. (2012). doi:10.1364/oe.20.023690.

[27] S.V. Yap, R.M. Ranson, W.M. Cranton, D. Koutsogeorgis, Decay time characteristics of la2O2S: Eu and la 2O2S: Tb for use within an optical sensor for human skin temperature measurement, Appl. Opt. (2008). doi:10.1364/AO.47.004895.

[28] X. xian Luo, W. he Cao, Ethanol-assistant solution combustion method to prepare La2O2S:Yb,Pr nanometer phosphor, J. Alloys Compd. (2008). doi:10.1016/j.jallcom.2007.06.011.

[29] I. Kandarakis, D. Cavouras, Experimental and theoretical assessment of the performance of Gd2O2S: Tb and La2O2S:Tb phosphors and Gd2O2S:Tb-La2O2S:Tb mixtures for X-ray imaging, Eur. Radiol. (2001). doi:10.1007/s003300000715.

[30] R.H. Krauss, R.G. Hellier, J.C. McDaniel, Surface temperature imaging below 300 K using La_2O_2S:Eu, Appl. Opt. (1994). doi:10.1364/ao.33.003901.

[31] C. Freiburg, W. Krumpen, U. Troppenz, Determinations of Ce, Eu and Tb in the electroluminescent materials Gd2O2S and La2O2S by total-reflection X-ray spectrometry, Spectrochim. Acta Part B At. Spectrosc. (1993). doi:10.1016/0584-8547(93)80032-P.

[32] J.A. Bagilo, Lanthanum Oxysulfide as a Catalyst for the Oxidation of CO and COS by SO2, Ind. Eng. Chem. Prod. Res. Dev. (1982). doi:10.1021/i300005a007.

[33] W.I. Dobrov, R.A. Buchanan, Photoconductivity and luminescence in lanthanum oxysulfide, Appl. Phys. Lett. (1972). doi:10.1063/1.1654343.

[34] Y. Yan, X. Zhang, H. Li, Y. Ma, T. Xie, Z. Qin, S. Liu, W. Sun, E. Lewis, An optical fiber

sensor based on La2O2S:Eu scintillator for detecting ultraviolet radiation in real-time, Sensors (Switzerland). (2018). doi:10.3390/s18113754.

[35] L. Wang, X. Yang, Q. Zhang, B. Song, C. Wong, Luminescence properties of La2O2S:Tb3+ phosphors and phosphor-embedded polymethylmethacrylate films, Mater. Des. (2017). doi:10.1016/j.matdes.2017.04.003.

[36] S.W. Kim, T. Hasegawa, T. Abe, H. Nakagawa, S. Hasegawa, K. Seki, K. Toda, K. Uematsu, T. Ishigaki, M. Sato, Abnormal improvement in emission of lanthanum oxysulfide phosphor La2O2S:Tb3+ synthesized by a novel method, thermal decomposition in eutectic molten salt, Ceram. Int. (2016). doi:10.1016/j.ceramint.2016.03.176.

[37] J. Fernández, R. Balda, M. Barredo-Zuriarrain, O. Merdrignac-Conanec, N. Hakmeh, S. García-Revilla, M.A. Arriandiaga, Spectroscopic and thermal study of Er-doped oxysulfide crystal powders, in: Laser Refrig. Solids VIII, 2015. doi:10.1117/12.2076963.

[38] D. Ma, S. Liu, Y. Zhang, C. Zhang, S. Huang, Controlled synthesis of Eu3+-doped La2O2S nanophosphors by refluxing method, J. Exp. Nanosci. (2013). doi:10.1080/17458080.2011.591002.

[39] M. Pokhrel, A.K. Gangadharan, D.K. Sardar, High upconversion quantum yield at low pump threshold in Er 3+/Yb3+ doped La2O2S phosphor, Mater. Lett. (2013). doi:10.1016/j.matlet.2013.02.062.

[40] L. Yu, F. Li, H. Liu, Fabrication and photoluminescent characteristics of one-dimensional La 2O2S:Eu3+ nanocrystals, J. Rare Earths. (2013). doi:10.1016/S1002-0721(12)60285-3.

[41] E.I. Sal'Nikova, D.I. Kaliev, P.O. Andreev, Kinetics of phase formation upon the treatment of La2(SO 4)3 and La2O2SO4 in a hydrogen flow, Russ. J. Phys. Chem. A.

(2011). doi:10.1134/S0036024411120296.

[42] Z. Liu, X. Sun, S. Xu, J. Lian, X. Li, Z. Xiu, Q. Li, D. Huo, J.G. Li, Tb3+- and Eu3+-doped lanthanum oxysulfide nanocrystals. Gelatin-templated synthesis and luminescence properties?, J. Phys. Chem. C. (2008). doi:10.1021/jp0764687.

[43] D. Qilin, S. Hongwei, W. Meiyuan, B. Xue, D. Biao, Q. Ruifei, Q. Xuesong, Z. Hui, Size and concentration effects on the photoluminescence of La 2O2S:Eu3+ nanocrystals, J. Phys. Chem. C. (2008). doi:10.1021/jp808343f.

[44] K. Ikeue, T. Kawano, M. Eto, D. Zhang, M. Machida, X-ray structural study on the different redox behavior of La and Pr oxysulfates/oxysulfides, J. Alloys Compd. (2008). doi:10.1016/j.jallcom.2007.04.145.

[45] K. Rajamohan Reddy, K. Annapurna, N. Sooraj Hussain, S. Buddhudu, Fluorescence spectra of Tb^{3+}: Ln<inf>2</inf>O<inf>2</inf>S powder phosphors, Spectrosc. Lett. (1997).

[46] T. Xia, W.H. Cao, X.X. Luo, Y. Tian, Combustion synthesis and spectra characteristic of Gd2O2S: Tb3+ and La2O2S: Eu3+ x-ray phosphors, J. Mater. Res. (2005). doi:10.1557/JMR.2005.0301.

[47] H. Peng, S. Huang, F. You, J. Chang, S. Lu, Lin Cao, Preparation and surface effect analysis of trivalent europium-doped nanocrystalline La2O2S, J. Phys. Chem. B. (2005). doi:10.1021/jp0453414.

[48] K. Rajamohan Reddy, K. Annapurna, S. Buddhudu, Fluorescence spectra of Eu3+:Ln2O2S (Ln = Y, La, Gd) powder phosphors, Mater. Res. Bull. (1996). doi:10.1016/0025-5408(96)00129-8.

[49] J. Ma, M. Fang, N.T. Lau, On the synergism between La2O2S and CoS2 in the reduction

of SO2 to elemental sulfur by CO, J. Catal. (1996). doi:10.1006/jcat.1996.0024.

[50] S. Buddhudu, F.J. Bryant, Optical transitions of erbium(3+):lanthanum oxide sulfide (La2O2S) and erbium(3+):yttrium oxide sulfide (Y2O2S)., J. Less-Common Met. (1989). doi:10.1016/0022-5088(89)90195-1.

[51] Y. Kitazawa, Y. Kunimoto, M. Wakihara, M. Taniguchi, Phase equilibria and oxidation mechanisms in the LA-S-O system, J. Therm. Anal. (1982). doi:10.1007/BF01912953.

[52] K.C. Bleijenberg, F.A. Kellendonk, C.W. Struck, Two-photon excited luminescence of thulium-activated lanthanum oxysulfide (La2O2S-Tm3+), J. Chem. Phys. (1980). doi:10.1063/1.440583.

[53] H. Ratinen, X-ray-excited optical fluorescence of ten rare earth ions in Y2O2S, La2O2S, and Gd2O2S, Phys. Status Solidi. (1972). doi:10.1002/pssa.2210120211.

[54] R. Ward, J.J. Pitha, A.L. Smith, The Preparation of Lanthanum Oxysulfide and its Properties as a Base Material for Phosphors Stimulated by Infrared1, J. Am. Chem. Soc. (1947). doi:10.1021/ja01200a009.

[55] X. Wang, J.G. Li, M.S. Molokeev, Q. Zhu, X. Li, X. Sun, Layered hydroxyl sulfate: Controlled crystallization, structure analysis, and green derivation of multi-color luminescent (La,RE)2O2SO4 and (La,RE)2O2S phosphors (RE = Pr, Sm, Eu, Tb, and Dy), Chem. Eng. J. (2016). doi:10.1016/j.cej.2016.05.089.

[56] J. Tauc, R. Grigorovici, A. Vancu, Optical Properties and Electronic Structure of Amorphous Germanium, Phys. Status Solidi. (1966). doi:10.1002/pssb.19660150224.

[57] V. Kumar, J.K. Singh, Model for calculating the refractive index of different materials, Indian J. Pure Appl. Phys. (2010).

[58] W.T. Carnall, G.L. Goodman, K. Rajnak, R.S. Rana, A systematic analysis of the spectra

of the lanthanides doped into single crystal LaF3, J. Chem. Phys. (1989). doi:10.1063/1.455853.

[59] C. Gorller-Walrand, K. Binnemans, Spectral intensities of f-f transitions.pdf, in: Handb. Phys. Chem. Rare Earths Vol 25, 1998.

[60] Advances in Spectroscopy for Lasers and Sensing, 2006. doi:10.1007/1-4020-4789-4.

[61] G.H. Dieke, H. Crosswhite, Spectra and Energy Levels of Rare Earth Ions in Crystals, che.13,InterscienceePublishers,1968.